


Article

Influence of Traction Battery Arrangement on Risk of Thermal Runaway and Loads Suffered by Electric Vehicle Occupant during Side Collision

Ana Olona ¹, Luis Castejón ^{2,*}  and David Valladares ²

¹ Research Department, Electric Vehicle and Mobility Area, Instituto de Investigación Sobre Vehículos, S.A., Ctra. N232, km 273, 50690 Zaragoza, Spain; a.olona@centro-zaragoza.com

² Department of Mechanical Engineering, University of Zaragoza, C/María de Luna s/n, 50018 Zaragoza, Spain; valladar@unizar.es

* Correspondence: luiscast@unizar.es; Tel.: +34-976762556

Abstract: In the current electric vehicles, the purpose of the traction battery is to store energy. When designing this battery, different parameters are considered to arrange the battery/module/cells in the mechanically and thermally safest configuration. Moreover, the battery layout must produce correct dynamic behavior during collisions. In the present study, different battery configurations plus added energy absorbers were analyzed. To achieve this, an internal combustion vehicle modeled with finite elements was applied as the reference model. The structural behavior of the different battery configurations in the event of a side collision was examined. First, the safest arrangement was established with respect to both cabin intrusion and thermal runaway propagation. Second, the safest arrangement that guarantees the safety of the occupants in the event of a side collision was analyzed using MADYMO. This software includes experimentally validated dummies that allow insight into the stresses experienced by occupants. The results of the analysis showed that battery pack inclusion in the vehicle increases the stiffness of the car floor, resulting in fewer intrusions into the passenger compartment. Therefore, safety of the occupants is increased. However, none of the configurations analyzed showed sufficient safety against thermal runaway. This study contains sufficient contributions to the new body of knowledge, since there is no study that analyzes the safest configuration in terms of battery behavior with respect to intrusion into the passenger compartment and the effect of thermal runaway, together with the fact that this is the safest configuration for occupants after analyzing the injuries they experience in a side collision for the different configurations.

Keywords: thermal runaway; electric vehicle battery; side collision



Citation: Olona, A.; Castejón, L.; Valladares, D. Influence of Traction Battery Arrangement on Risk of Thermal Runaway and Loads Suffered by Electric Vehicle Occupant during Side Collision. *Energies* **2023**, *16*, 6892. <https://doi.org/10.3390/en16196892>

Academic Editors: Byoung Kuk Lee and Hugo Morais

Received: 28 June 2023

Revised: 14 September 2023

Accepted: 26 September 2023

Published: 29 September 2023



Copyright: © 2023 by the authors. Licensee MDPI, Basel, Switzerland. This article is an open access article distributed under the terms and conditions of the Creative Commons Attribution (CC BY) license (<https://creativecommons.org/licenses/by/4.0/>).

1. Introduction

A vehicle must comply with a series of regulations and norms. In addition to these regulations, several private programs assess vehicle safety. These include the NCAP programs (Euro NCAP, US NCAP, J NCAP, etc.), the tests of which are not mandatory. In most current electric vehicles (EVs), the battery pack is placed in the primary safe zone [1]. In this study, the battery pack was placed in the secondary safe zone to ensure interaction with the crumple zone of the vehicle. In addition, the battery pack needs appropriate protection mechanisms in the event of a side collision. EVs provide propulsion by efficiently transforming the energy stored in the traction battery into electrical energy. However, EVs face major challenges associated with range, weight, and safety. In particular, the safety of the battery during a side collision is a concern for EVs. Based on data from real-world accidents and laboratory crash tests, two safe zones are defined in a vehicle based on intrusion data from vehicles experiencing real accidents and laboratory crash tests [1], a primary safe zone and a secondary safe zone. The vehicle passenger compartment is

contemplated as a primary safe zone and it is a safe zone against impacts, and the rest of the vehicle's platform is considered as a secondary safe zone.

In the event of an impact, certain vehicle components absorb large amounts of deformation energy, which is transformed from the kinetic energy of the impact. In the event of a side collision in an electric vehicle (EV), the space available to absorb the energy is reduced to the area between the body and the battery pack.

A lithium-ion battery can fail due to mechanical, electrical, or thermal failure at the cell, module, or battery pack level (Figure 1). These failures happen as a successive series, which leads to the thermal runaway phenomenon. Mechanical failure may occur due to collision, deformation, or puncture, which may cause an internal short circuit and high internal heat. With increasing temperature, many exothermic reactions occur. Finally, if the heat is not controlled, feedback occurs, and thermal runaway occurs. In the case of battery deformation, the separator deforms, which may cause an internal short circuit, or the electrolyte liquid may leak and cause a fire. During a collision, a battery puncture may occur, which is usually more serious than a deformation, resulting, in many cases, in thermal runaway as well. Electric failure can be caused by an external short circuit, overload, or overdischarge, which are mainly due to poor control of the battery management system (BMS). An external short circuit can occur when the electrodes are connected by a conductor during a collision or by water entering the battery. Overcharge and overdischarge do not always cause thermal runaway but commonly lead to the degradation of the storage capacity of the cell and, thus, of the battery. In the case of overdischarge, the BMS fails to stop the charging process at the maximum voltage limit; consequently, heat and gas are generated. In the case of overdischarge, the BMS fails to correctly limit cell usage at minimum voltage levels, resulting in increased heat and gas generation and cell swelling. Finally, thermal failure can occur due to overheating, which may be caused by incorrect contact connections or excessive heat in the vicinity of the battery pack, such as from a fire caused by a car accident. Moreover, overheating can occur during fast charging with a supercharger. This failure can also be caused by an internal short circuit, which occurs because of cell separator failures, contamination, manufacturing defects, or dendrite formation (lithium build-up) at the anode. This failure may also occur due to defects during cell manufacture that cause an internal short circuit.

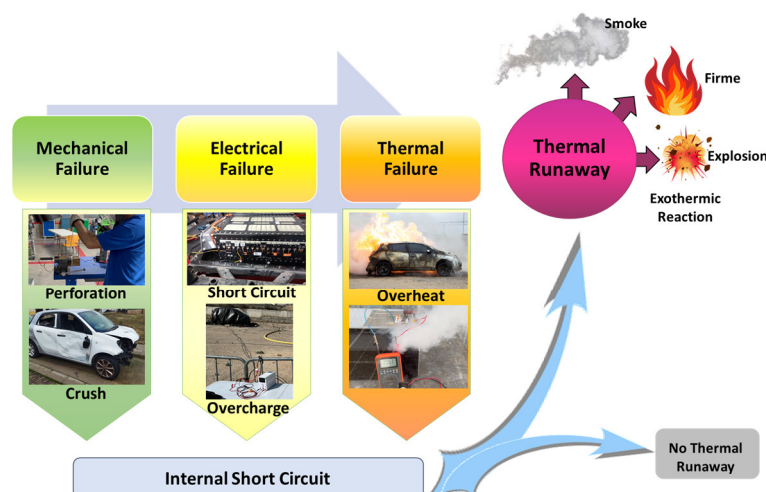


Figure 1. Thermal runaway mechanism of lithium-ion battery for EVs [2].

This inherent feature of high-voltage batteries necessitates the reinforcement of the traction battery casing and the inclusion of elements capable of absorbing the energy produced during the collision to prevent damage to the battery cells.

According to published data [3], in 2022, 11.5% of interurban road casualties in Spain occurred in a side or frontal-side collision; in these types of collisions, compared with a frontal collision, there is much less space inside the vehicle to absorb energy. Therefore, serious head and chest injuries are common with side impacts, being more severe than in frontal collisions.

The reason for this is that the body of the driver is closer to the impacting car and/or the internal structures of the door are deformed, resulting in their intrusion, which directly strike the hemithorax close to the impact side. Side impact tests with a movable deformable barrier simulate the collision were a vehicle strikes the side of a second vehicle. In this test, a trolley with a deformable barrier with the physical characteristics of a real vehicle is launched against a vehicle, imitating its behavior and stiffness, at a given speed and angle. These tests are defined in official regulations. Depending on the type of test and the standard in which it is described, the characteristics of the collision vary (speed of the crash element, angle of impact). The U.S. standard is Federal Motor Vehicle Safety Standard (FMVSS) 214, defining an impact speed of the crash barrier of 53.9 km/h, a barrier weight of 1361 ± 4.5 kg, and an impact angle of 27° [4].

The standards applied in this study were those outlined in the United Nations Regulation No. 95, Uniform provisions concerning the approval of vehicles regarding the protection of the occupants in the event of a side collision [5], describing the side impact test procedure (Figure 2). Side impacts cause many fatalities and serious injuries, accounting for approximately one-quarter of all crashes. Euro NCAP has been conducting testing on the driver side of since its inception. However, almost half of the occupants injured in side impacts are sitting opposite the struck side. In a side impact, both occupants on the struck (near) side and occupants on the opposite (far) side of the vehicle are at risk of injury. Specifically, impacts on the opposite side account for 9.5% of all car accidents and 8.3% of all MAIS+3 injuries experienced by occupants [6]. The head and thorax are the most commonly injured body regions. As the most head injuries occur to those sitting on the side on which the vehicle is struck [7], establishing measures to reduce vehicle intrusion and head excursion is essential to reduce injuries. Currently, some automobile manufacturers are addressing these opposite-side impacts and introducing countermeasures, such as a central airbags, to mitigate the injuries that could occur. In this study, we analyzed injuries to the front passenger, receiving the impact on the right side of the vehicle. Different dummies can be used to analyze the protection of provided by vehicles in a lateral collision. Of these, the male WorldSID dummy is more biofidelic than the ES-2re dummy, and its level of biofidelity is acceptable for the technical regulations on side impact. We conducted a parametric evaluation of the effect of a side impact on the kinematics of a dummy, which we analyzed on a EuroSID 2, for five different vehicle configurations. The test conditions followed those established in ECE Regulation R95, in which the ES-2 dummy (EuroSID 2) is used.

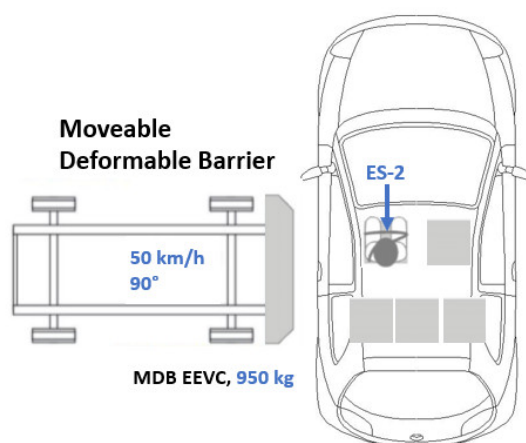


Figure 2. Diagram of side collision test with movable barrier according to ECE Regulation R95 [5].

2. Materials and Methods

2.1. Methodology

We evaluated the safety of different electric vehicle configurations, by means of by correlating the simulation results with the thresholds set out in ECE Regulation R95. The reference car model was a combustion engine car (Geo Metro 3-Door Gen II) (Figure 3a), modeled with finite elements (Figure 3b), including a mobile barrier. The side impact was simulated according to Directive 97/26/EC.

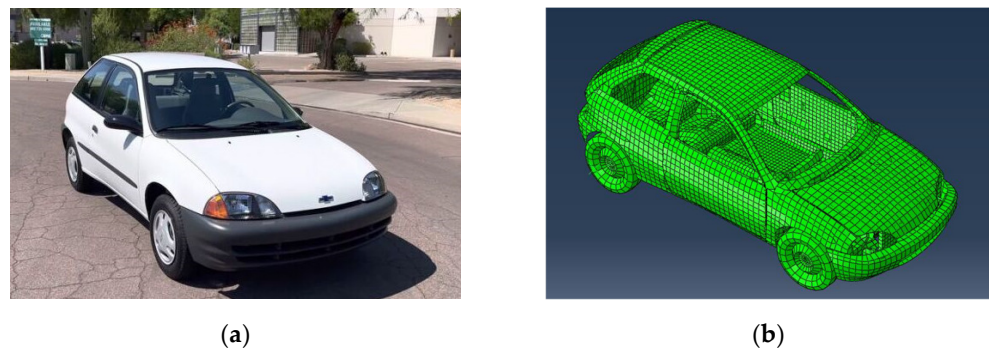


Figure 3. (a) Geo Metro 3-Door Gen II model; (b) Geo Metro 3 model modeled with finite elements. Model used as a reference.

This model was converted to an electric vehicle by introducing two different traction battery configurations; subsequently, the vehicle floor and area under bench of the reference vehicle (Figure 4a) has adapted for an electric vehicle (Figure 4b) and some absorbers were applied. A real battery of a first-generation Nissan Leaf was taken as a reference (48 modules 24 kWh), containing 48 modules with 4 cells each. The materials applied in this real battery were via measurements from some samples from the battery.

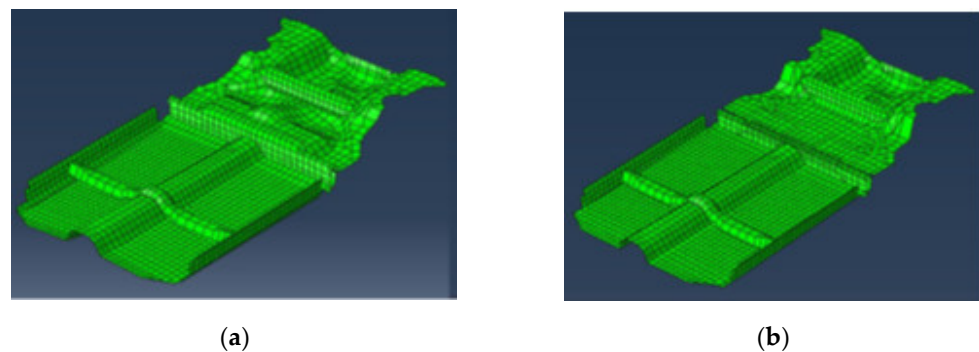


Figure 4. (a) Vehicle floor and area under rear bench of the reference vehicle; (b) adapted electric vehicle floor and area under rear bench to create room for the traction battery.

We used a battery with 28 modules with 4 pouch cells each. Some cells with higher energy density, such as prismatic and cylindrical cells, are safer [8]. However, pouch cells were selected because they are commonly used in most electric vehicles. The least favorable scenario was studied. In total, four different electric vehicle configurations were analyzed; each of them is explained below.

2.1.1. Electric Vehicle Configuration 1

A high-voltage battery was designed based on maximizing the use of the available space on the floor and under the rear bench and minimizing the increase in floor height under occupants' feet (Figure 5a). The separation between the modules and the housing wall was 50 mm, which is the recommended dimension to avoid damage to cells in case of impact [9]. The high-voltage battery housing was modeled in two parts: the bottom and top housing, reproducing a real battery scheme. The modules were characterized according to the technical data of the Nissan Leaf battery [10]. The battery dimensions were $303 \times 223 \times 55$ mm. The inner volume of the modules was modeled with these measures as a solid. The battery housing was represented with a 0.5 mm thickness and the same overall dimensions. Moreover, a $245 \times 135 \times 30$ mm space was reserved on one side of the modules to represent the space occupied by the battery management system (BMS). However, the BMS was not implemented in the finite element model. This did not interfere with the results obtained from the simulation because the BMS is located on the side opposite from the impact.

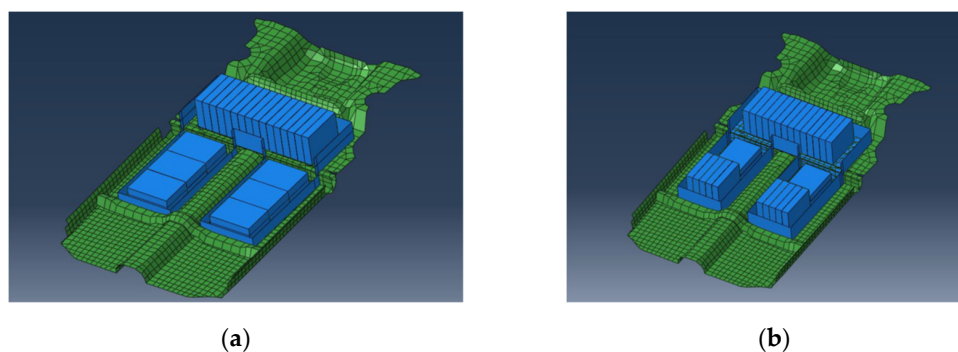


Figure 5. High-voltage battery layout in EV (a) configuration 1; (b) configuration 2.

2.1.2. Electric Vehicle Configuration 2

In this second configuration, the results of a study on the propagation of thermal runaway were considered [11]. The authors of this study stated that the possibility of the propagation of thermal runaway is higher in the vertical than in the horizontal arrangement. In addition, the importance of the spaces between packages and their cooling to ensure safe operation was highlighted, which reduce the likelihood of a loss of heat transfer control in the battery assembly. In this configuration, protection against thermal runaway is improved because the modules on the floor of the vehicle are reorganized (Figure 5b), and the overall width of the assembly is reduced, leaving more space for possible lateral shock absorbers. In this configuration, 90 mm of space exists at both battery set sides, which is larger than the 50 mm in configuration 1.

The method of modeling the battery housing was the same as that in configuration 1, with the dimensions adapted to the new battery layout. The modules, their respective housings, and the BMS had the same dimensions as in configuration 1.

2.1.3. Electric Vehicle Configuration 3

With both configurations 3 and 4, we aimed to improve the battery protection in the event of a collision by implementing shock-absorbing elements on both sides of the housing, adapting their dimensions to the battery housing shape and the available space.

Based on prior results [12], in which three alternatives for different shock absorbers were compared, the material chosen for these new components was aluminum foam (Table 1).

Table 1. Properties of aluminum foam.

Density (kg/m ³)	390
Young's modulus (GPa)	0.175
Poisson's ratio (-)	0.05

Configuration 3 corresponds to configuration 1 with the addition of absorbers (Figure 6a). In configuration 1, less space was available on the sides of the battery, as the placement was lower on the vehicle floor and was therefore wider. In this case, the maximum absorber width was 10.9 cm.

2.1.4. Electric Vehicle Configuration 4

Configuration 4 was configuration 2 to which shock absorbers were added (Figure 6b). In configuration 2, the battery distribution was higher above the vehicle floor and allowed for a narrower housing. Therefore, the shock absorbers had a maximum width of 14 cm (3.1 cm wider than in configuration 3).

The following Figure 7 shows a comparison of the four different electric vehicle configurations that will be analyzed.

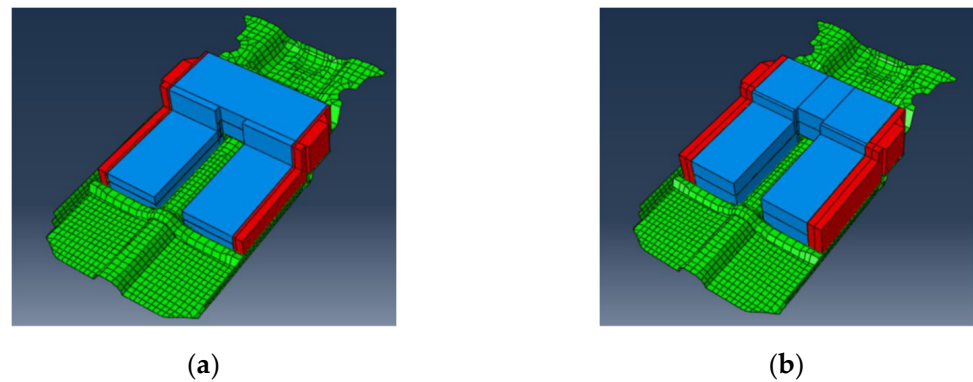


Figure 6. (a) Configuration 3: configuration 1 with shock absorbers; (b) configuration 4: configuration 2 with shock absorbers.

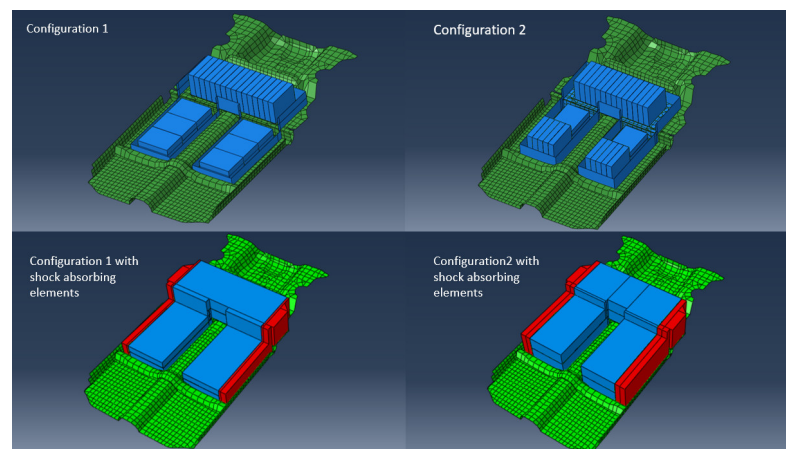


Figure 7. Comparison of four electric vehicle configurations analyzed.

2.2. Characterization of Battery Materials

For the finite element modeling of a traction battery to conduct simulations with various computer programs, we needed to characterize the battery materials. To this end, Vickers microhardness tests were carried out on a sample of both the upper and lower cover of the original battery casing and the module casings to determine their mechanical properties for their introduction into the simulation program. On the other hand, to characterize the material inside the modules, we determined the composition of the four cells of the bag that composed the modules.

The Vickers test is based on an optical measuring system. A diamond indenter shaped similar to a square pyramid is used to perform the microhardness test. The indenter is used to penetrate the material studied, with a known load and for a period that is usually between 10 and 15 s. Subsequently, the length of the diagonal of the indentation left by the diamond indenter is measured with a microscope to calculate the area of the inclined surface of the indentation. With these data, the Vickers hardness can be calculated as the quotient between the load applied during the test and the indentation area (Figure 8).

We collaborated with the Materials Department of the University of Zaragoza to complete this test. First, specimens with the necessary dimensions for the tests were obtained (Figure 9).

The conducted tests are shown below (Figures 10 and 11).

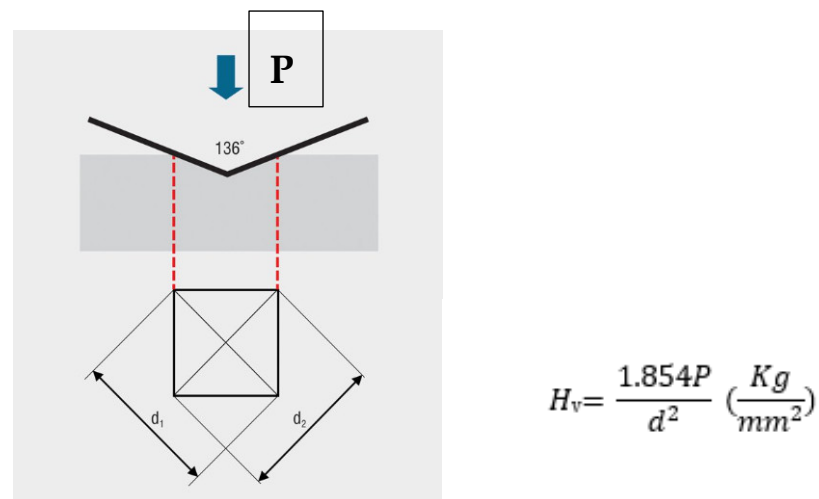


Figure 8. Explanation of the Vickers microhardness test.

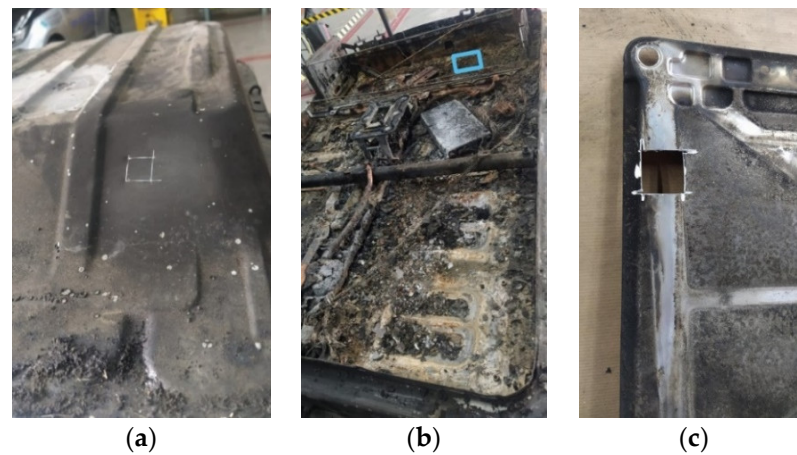


Figure 9. Test specimen obtained from the (a) upper and (b) lower casing of the high-voltage battery, and from the (c) casing of a high-voltage battery module.

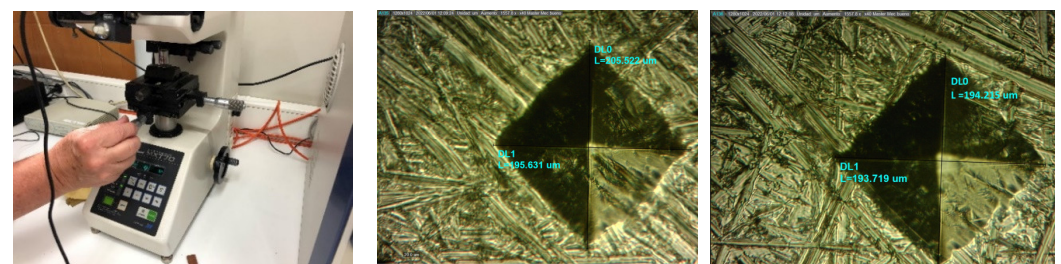


Figure 10. Views of the Vickers test on specimen from upper casing of high-voltage battery.

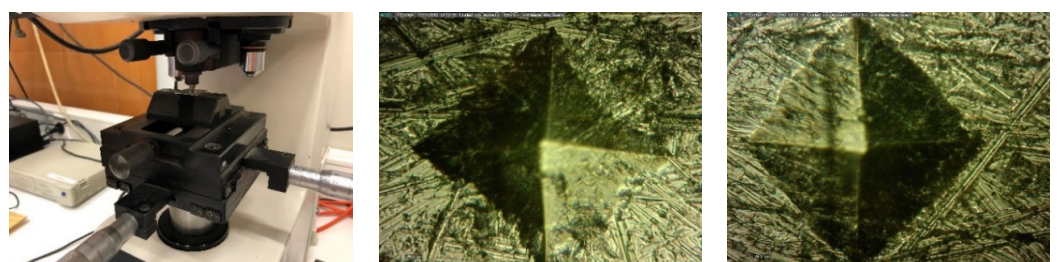


Figure 11. Views of the Vickers test on high-voltage battery module housing specimen.

The results obtained in each of the tests (two per specimen) are shown in Table 2.

Table 2. Results of Vickers microhardness tests on different specimens.

	P (kg)	d ₁ (mm)	d ₂ (mm)	HV (kg/mm ²)
Upper housing cover	0.5	0.094941	0.1956	108.005069
	0.5	0.0897204	0.1937	115.480832
				111.742951
Lower housing cover	0.5	0.094941	0.2031	104.076514
	0.5	0.0903672	0.1962	113.193268
				108.634891
Module housing	0.5	0.1103256	0.2582	70.3455591
	0.5	0.114807	0.2409	72.5473466
				71.4464529

Based on the results of the microhardness tests on both the upper and lower casing covers, a hardness of 110 kg/mm² was obtained. According to the interpretation in the conversion tables [13], a mechanical strength of 53 psi was deduced. Applying the conversion factor (6.9 N/mm² per psi unit), we obtained a mechanical strength of 365.7 N/mm². The yield strength can be also approximated as three times the Vickers hardness, i.e., 330 MPa. With these results, we compared the various materials that can be used to manufacture the casing, among which the low-carbon steels DC01, DC02, and DC03 were compared [14]. We chose hardened DC01, which has a yield strength of 200–380 N/mm² and a mechanical strength of 290–430 N/mm². The properties used to define the steel chosen are listed in Tables 3 and 4.

Table 3. Properties of DC01 steel [15].

Density (kg/m ³)	7850
Young's modulus (GPa)	210
Poisson's ratio (-)	0.3

Table 4. Plastic behavior of DC01 steel.

Yield and Ultimate Strength (MPa)	Associated Plastic Strain
330	0
365.7	0.18

The same procedure was applied for the individual module housings, producing a Vickers hardness of 71 kg/mm², a yield strength of 213 MPa (three times the Vickers hardness), and a mechanical strength of 227.7 MPa. Several aluminum alloys and low carbon steels were compared, and the aluminum alloy 6063-T6 was chosen, which had a yield strength of 215 MPa and a mechanical strength of 240 MPa. The properties used to define the chosen aluminum 6063-T6 [16] are listed in Tables 5 and 6.

Table 5. Properties of aluminum 6063-T6.

Density (kg/m ³)	2700
Young's modulus (GPa)	69
Poisson's ratio (-)	0.33

Table 6. Plastic behavior of aluminum 6063-T6.

Yield and Ultimate Strength (MPa)	Associated Plastic Strain
215	0
240	0.10

The content of the modules was defined by calculating the equivalent properties from the components of the four pouch cells inside them. These modules had a graphite anode and a LiMn_2O_4 cathode with LiNiO_2 [10]. Both separator foils and cell envelopes were neglected. LiMn_2O_4 and LiNiO_2 were assumed to have the same characteristics, and the properties of the anode and cathode were weighted with a coefficient of 0.5 each. Based on previously collected data [17], the properties of the equivalent module material were obtained, and they are summarized in Table 7.

Table 7. Equivalent properties of interior of modules.

	LiMn_2O_4 (25%)	LiNiO_2 (25%)	Graphite (50%)	Equivalent Module Material
Density (kg/m^3)	4140	4650	2300	3347.5
Young's modulus (GPa)	194	194	109	151.5
Poisson's ratio (-)	0.26	0.26	0.24	0.25

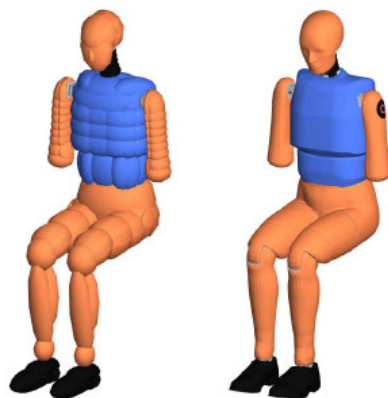
2.3. Occupant Injury Analysis

This vehicle model was imported into MADYMO software (MATHematical DYnamic MOdel) version 2212. MADYMO is software that allows the analysis of the injuries suffered by the occupants in a collision and to determine their origin. It is used to determine the behavior of occupant restraint systems (seat belts, airbags, and head restraints).

In this study, MADYMO was used to analyze the movement and stresses experienced by a right front occupant in a vehicle involved in a collision on the right side, with reference to the running direction. For this purpose, the vehicle was fitted with a seat on which the dummy was located. The dummy movement and the stresses it experienced because of the lateral collision were analyzed. The seat belt was also modeled.

2.3.1. The Dummy Model

We conducted a parametric evaluation of the effect of a side impact on the kinematics of a dummy. For this purpose, a EuroSID 2 was used for each of the five vehicle configurations analyzed. The test conditions were those established in the ECE Regulation R95, in which the ES-2 dummy (EuroSID 2) is applied. The models used by MADYMO are shown below (Figure 12). They were calibrated and validated using numerous impact tests on components and complete dummies.

**Figure 12.** ES-2(re) ellipsoid dummy (left), used in the simulation, and ES-2(re) faceted dummy (right) in its reference position [18].

2.3.2. The Vehicle Model

For the analysis, the car model was imported (for the five configurations), and the seat was fitted (Figure 13). In addition, the stresses experienced by the right front occupant, with reference to the running direction, were analyzed.

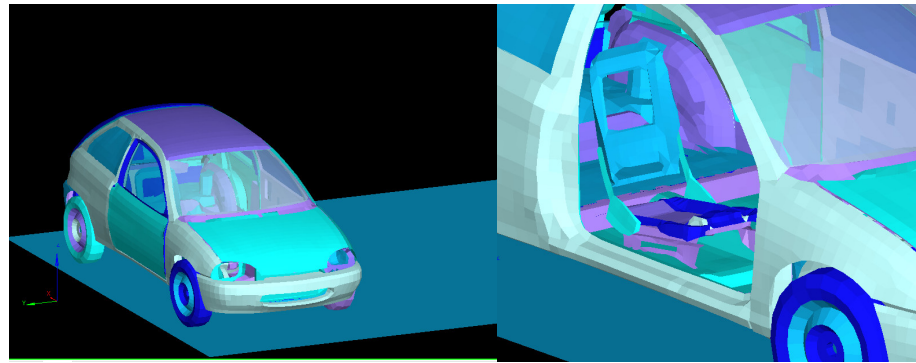


Figure 13. Image of the vehicle used, and details of the seat fitted for the dummy.

2.3.3. Lateral Crash Test with Deformable Barrier

The side crash test with a deformable barrier was analyzed according to the UN ECE R95 standard. This test simulates a side crash between two cars at a given relative angle, as might occur at a road junction, for example. To perform this test, a vehicle to be tested, a movable deformable barrier, and dummies are required. A deformable barrier with the characteristics of the barrier used in the ECE Regulation R95 was added to the above model.

In FMVSS 214, the ES-2 re dummy is used; in UN R95, the ES-2 dummy is used; and in EuroNCAP, the WorldSID dummy is used. For this reason, the ES-2 dummy was applied following ECE Regulation R95.

Figure 14 shows the whole model that was simulated including the corresponding dummy and the seat belt.

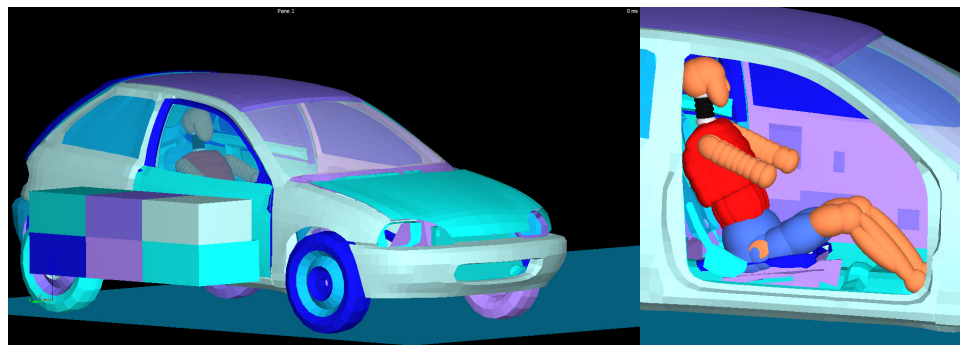


Figure 14. Whole model that was simulated according to ECE Regulation R95 using the EuroSID-2 dummy.

3. Results and Discussion

The behavior of the different configurations was analyzed by FEM (Finite Element Method) to determine the optimum configuration in terms of occupant safety, intrusion into the passenger compartment, and thermal runaway propagation.

First, the instant of maximum deformation for each of the configurations was analyzed (Table 8), which considerably reduced when the battery pack was installed, as the vehicle was transversely stiffened. After including the shock absorbers, a decrease in the time before reaching the moment of maximum deformation was also observed, as these new components also added stiffness to the car.

Table 8. Comparison of instant of maximum deformation of the car model.

	Without Battery	Config. 1	Conf. 2	Config. 1 with Shock-Absorbing Elements	Config. 2 with Shock-Absorbing Elements
Time of maximum deformation(s)	0.1	0.0615	0.0625	0.056	0.058

The upper view for each of the five configurations at the moment of maximum deformation is shown in Figure 15.

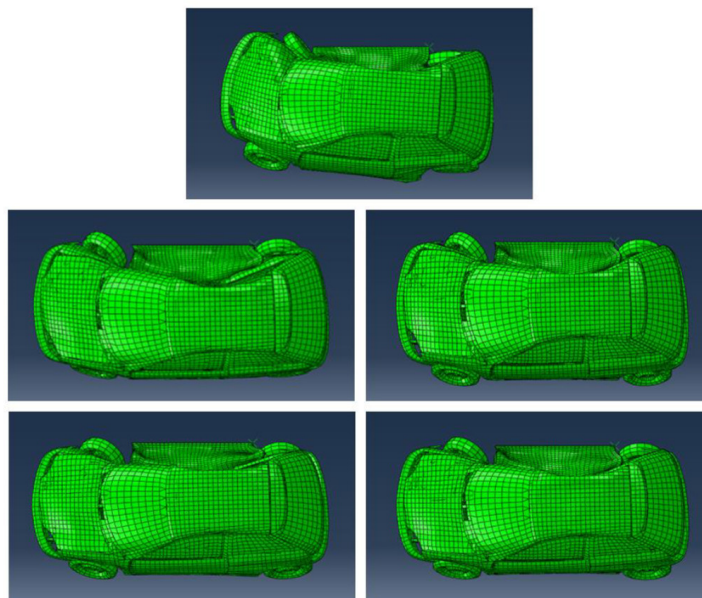


Figure 15. Deformed car model at the instant of maximum deformation. From left to right and from top to bottom: configuration without battery, configuration 1, configuration 2, configuration 1 with absorbers, and configuration 2 with absorbers.

Table 9 shows the maximum velocity and acceleration for each of the five configurations. Because the mass of the vehicle increases with the inclusion of the battery pack, and applying the conservation of linear momentum, the maximum velocity and acceleration after impact for the configurations with battery pack decrease.

Table 9. Comparison of maximum speed and acceleration.

	Without Battery	Config. 1	Conf. 2	Config. 1 with Shock-Absorbing Elements	Config. 2 with Shock-Absorbing Elements
Maximum Velocity (m/s)	10.09	7.52	7.35	7.77	7.73
Maximum Acceleration (m/s²)	876.49	291.12	310.65	427.49	360.06

Figure 16 shows the average velocity and the Figure 17 shows the average acceleration, both measured on vehicle floor during impact for each configuration analyzed.

Once the moment of maximum deformation is known, the maximum von Mises stress in the vehicle components that absorb energy in the impact between the barrier and the battery modules was analyzed to determine whether these elements have sufficient yield strength and whether they withstand the impact without breaking, comparing the maximum stress achieved with the yield strength and the ultimate strength (Table 10).

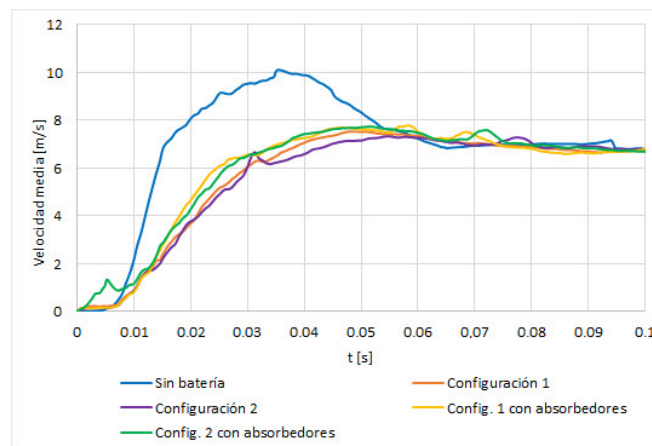


Figure 16. Average velocity (m/s) measured on vehicle ground during impact for each configuration.

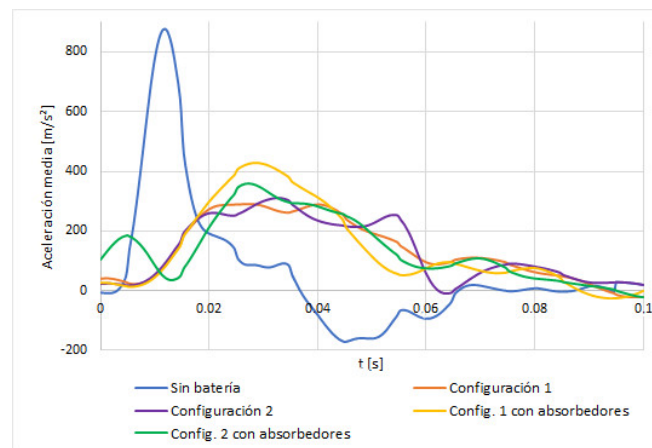


Figure 17. Average acceleration (m/s²) measured at vehicle floor during impact for each configuration.

Table 10. Comparison of protection elements.

		Without Battery	Config. 1	Config. 2	Config. 1 with Shock-Absorbing Elements	Config. 2 with Shock-Absorbing Elements
Side sill	$E_{\text{deformmax}}$ (J)	939.08	1472.23	1597.28	878.17	784.30
	$\sigma_{VM\text{max}}$ (MPa)	982.1 ¹	1089 ²	991.8 ¹	909.6 ¹	895.8 ¹
Housing	$E_{\text{deformmax}}$ (J)	-	2125.87	2515.62	1908.04	1782.96
	$\sigma_{VM\text{max}}$ (MPa)	-	365.7 ²	360.5 ¹	339.6 ¹	351.3 ¹
Shock absorber	$E_{\text{deformmax}}$ (J)	-	-	-	684.09	729.94
$\Sigma E_{\text{deformmax}}$ (J)		939.08	3598.1	4112.9	3470.31	3297.20

¹ The element stress is greater than yield strength. ² The element breaks.

In none of the configurations did plastic deformation of the modules occur; therefore, no breakage was observed. However, Table 11 shows that in all the models with a battery, thermal runaway occurs in the same type of module: those that are placed with the largest area facing the impact. Notably, this distribution is precisely the one recommended [11] to reduce the transmission of this phenomenon to different battery modules.

3.1. Thermal Runaway

It has sought to meet criteria that guarantee that the battery does not suffer damage that endangers the safety of passengers in relation to the phenomenon of thermal runaway.

Thermal runaway (TR) occurs when the temperature exceeds critical values due to a mechanical, electrical, or thermal failure. Collisions between vehicles (mechanical impact) can cause deformations that cause the battery to crush or break [2].

When a battery cell is subjected to mechanical impact, it is first mechanically deformed. If a mechanical failure of the separator or electrodes occurs, it can lead to a short circuit, to an increase in temperature, gas generation and a consequent increase in pressure [19].

Most of the research analyzed [19] has found a temperature rise in all the cells of a battery pack can occur due to structural deformation produced by an impact. The result of this deformation can also be a high probability of TR propagation from one cell to adjacent cells.

There are several studies on aspects that limit the applications of lithium-ion batteries [19], such as the risk of overcharging lithium-ion batteries, the reactions that occur inside these batteries and the propagation of heat generated in one cell to its adjacent cells. The findings of this studies [19] indicated that over-discharge can be dangerous for lithium-ion batteries because the voltage decreases below a threshold value.

There is a review article [20] about the application of ML (machine learning) for thermal management and for battery safety system. Three most common ML models have been analyzed: ANN (artificial neural networks), CNN (convolutional neural networks) and LSTM (short-term memory). LSTM is the best option to establish models to predict the temperature or to diagnose thermal risks with time series. In addition, the new DT (Digital Twin) technology is applied to battery safety and BTMs. This technology is very good for computation, data storage capacity and reliability of real-time simulation.

Since it is necessary for batteries to have a thermal management system with low energy consumption, high temperature regulation capability and uniform temperature maintenance, one study [21] discusses different options for lithium-ion battery thermal management control: measures to control the maximum temperature of the battery, proper charging and discharging temperature; regulate the temperature change; outer cooling system and procedures to protect. The main findings of this review [21] are:

1. Various problems related to heat generation and heat dissipation in battery packs were analyzed, and the thermal capacity and conductivity of the battery pack were also analyzed.
2. Different cooling strategies and various optimization methods were analyzed, within the thermal management technologies currently used.
3. The BTMS control strategy in battery packs is very important and can improve their performance by reducing energy consumption.
4. To optimize the design of the BTMS and select the most appropriate, different evaluation parameters used in previous studios of researching can be used.

Criteria are used to ensure that a battery is not damaged in a way that endangers vehicle occupant safety in relation to thermal runaway. A module can sustain a compressive force of 445 kN before thermal runaway occurs [22].

To convert these data into a criterion, a battery module with a shell and solid interior was modeled with the same characteristics as in the side impact model. This module was simulated in three different situations, each time receiving the corresponding force on one of the three different surfaces. This force was applied punctually at the nodes, so it was necessary to divide the force of 445 kN by the number of nodes defining the surface to be studied.

Subsequently, the obtained shortening was noted, which is the criterion considered when interpreting the results. If the shortening obtained in any of the battery configurations exceeds this value, the configuration is not safe against thermal runaway.

In the first configuration, the modules on the floor were placed horizontally on the floor, with the smallest surface (55 × 223 mm) facing the movable barrier. They were resting on the ground at their base, the largest surface area, and the impact hit the smallest surface area.

The maximum shortening that a module under compression can withstand on its smallest face ($\Delta l_{\text{minimum}}$) is 0.0699 mm. For larger deformations, thermal runaway occurs.

In the second configuration, the modules, which were placed horizontally on the vehicle floor, had the median surface perpendicular to the direction of movement of the moving barrier and rest on the larger surface.

The maximum shortening that a module whose median face is directed toward the impact (Δl_{mean}) can withstand is 0.037 mm before thermal runaway occurs.

Finally, we simulated the situation where the modules of both configurations are resting under the rear bench, placed on their edge, and part of those placed on the floor of the second configuration are also on their edge. These are in contact with the floor through the middle surface and in contact with other modules on their larger surface.

The maximum shortening of a module under compression on its largest surface ($\Delta l_{\text{maximum}}$) is 0.0094 mm; beyond this, thermal runaway occurs.

Consider these results, we concluded that the most critical module of configuration 1 with shock absorbers is close (within 0.0004 mm) to fulfilling the requirements to avoid thermal runaway. This makes it the best option among the four arrangements with a battery in this study. However, improvements can be applied that would reduce the fire hazard of the battery, which is described below.

Table 11. Comparison of module behavior [23].

	Config. 1	Config. 2	Config. 1 with Shock-Absorbing Elements	Config. 2 with Shock-Absorbing Elements
$E_{\text{deformmax}}$ (J)	154.48	1407.57	69.93	1370.20
$\sigma_{VM\text{max}}$ (MPa)	181.8	214.9	214.1	166.1
Modules shortening	$\Delta l_{\text{minimum}}$ (mm)	0.0061	-	0.0034
	Δl_{mean} (mm)	-	0.0239	-
	$\Delta l_{\text{maximum}}$ (mm)	0.0264 *	0.0417 *	0.0098 *
$\Sigma E_{\text{deformmax}}$ (J)	3598.1	4112.9	3470.31	3297.20

* The maximum shortening was exceeded.

3.2. Intrusion into Passenger Compartment of the Vehicle

Intrusion into the passenger compartment was measured with four different parameters, measured at the instant of maximum deformation in each of the cases analyzed, to determine the effect of the battery on the structural behavior of the vehicle during a side impact.

3.2.1. Intrusion at Side Sill

The first two parameters considered were the maximum distance and the average distance that different nodes penetrate at side sill height (Figure 18). These distances were calculated as the difference between the vehicle width before and after impact at different nodes.

We observed in Table 12 that both the battery and the absorbers stiffened the vehicle structure, as the intrusions were reduced. By including the battery, the floor was stiffened, and the side sill intrusions were considerably reduced. The intrusions were smaller in the case of configuration 1 as the battery was wider than in the case of configuration 2; therefore, a larger zone of the vehicle floor was stiffened.

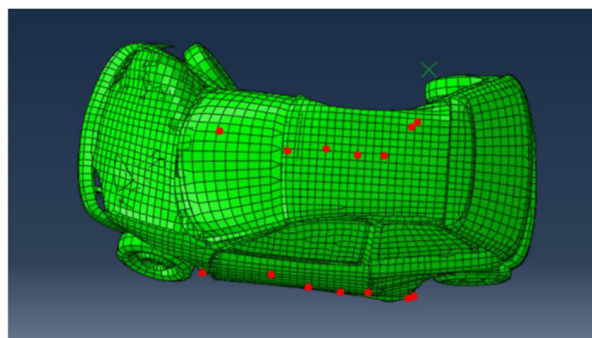


Figure 18. Nodes selected for calculation of $d_{T\text{max}}$ and $d_{T\text{mean}}$ at instant of maximum penetration.

Table 12. Comparison of protection elements.

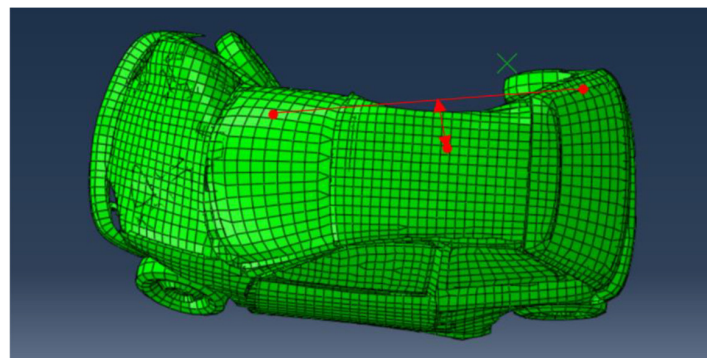
	Without Battery	Config. 1	Config. 2	Config. 1 with Shock-Absorbing Elements	Config. 2 with Shock-Absorbing Elements
$d_{Tmax}(mm)$	333.55	224.85	253.02	205.55	253.48
$d_{Tmax}(mm)$	252.60	128.86	160.31	93.87	100.67

By implementing shock absorbers, the average penetration into the passenger compartment at the side sill was further reduced. However, in the second configuration with absorbers, the maximum intrusion obtained between the nodes was almost the same as that without absorbers, whereas the average intrusion considerably decreased. This means that one of the nodes had a large deviation from the line of nodes; however, generally, the right side of the vehicle reduced the intrusion of its surface.

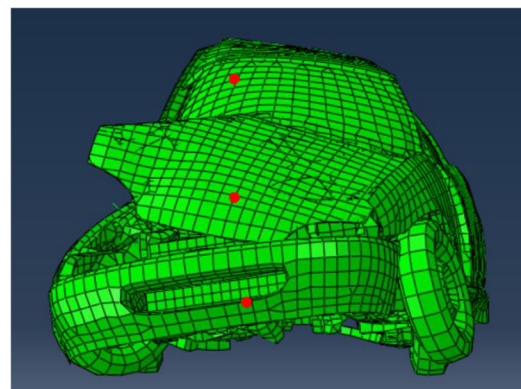
3.2.2. Intrusion at B Pillar

For this element, two different parameters were calculated to quantify the intrusion into the passenger compartment at the B pillar of the vehicle at the instant of maximum deformation.

The first, d_H , is defined as the distance that a B pillar node penetrates inside the passenger compartment with respect to the two nodes of the A and C pillars. The distances from this node to the imaginary line formed by two nodes on the A and C pillars of the vehicle at the same z-value, both before and after the impact (Figure 19), were calculated and summed to calculate the value of d_H .

**Figure 19.** Nodes selected for the calculation of d_H at the instant of maximum deformation.

The second parameters, d_V , is the distance penetrating the center of the B pillar in relation to its anchorages. It was calculated as the sum of the distances before and after the impact (Figure 20) from a node in the middle of the pillar to the imaginary line between two nodes each located at an anchorage of the pillar.

**Figure 20.** Nodes chosen for the calculation of d_V at the instant of maximum deformation. The best configuration was configuration 1 with absorbers (Config.1 with shock-absorbing elements).

When analyzing the intrusions on the B pillar of the vehicle (Table 13) by including the battery assembly, a reduction in d_H was achieved. After implementing the absorbers, this distance was further reduced. d_V slightly increased when the battery pack was fitted, as the floor did not deform as much as the rest of the side, and this intrusion was measured as a function of the distance from a node in the center of the pillar to the line formed by its anchorages. However, this distance decreased with the implementation of the absorbers.

Table 13. Intrusion at B pillar for the different configurations.

	Without Battery	Config. 1	Config. 2	Config. 1 with Shock-Absorbing Elements	Config. 2 with Shock-Absorbing Elements
d_H (mm)	351.48	222.91	238.96	160.19	120.95
d_V (mm)	101.32	103.71	108.85	85.30	81.24

3.3. Results for Different Electric Vehicle Configurations

The movement of the dummy and the stresses to which it was subjected were analyzed for the different vehicle configurations. The injury thresholds indicated by the regulations and the private programs that analyze vehicle safety were taken as the reference values. The test configuration used was ECE Regulation R95.

Below is a sequence of frames showing the movement experienced by the passenger of a vehicle subjected to an acceleration similar to that experienced in a lateral collision according to ECE Regulation R95. The passenger is located on the right-hand side of the vehicle related to the running direction.

3.3.1. Passenger Kinematics in a Combustion Engine Vehicle

Figure 21 shows a sequence of frames showing the movement experienced by the passenger of a combustion vehicle subjected to a lateral collision according to ECE Regulation R95.

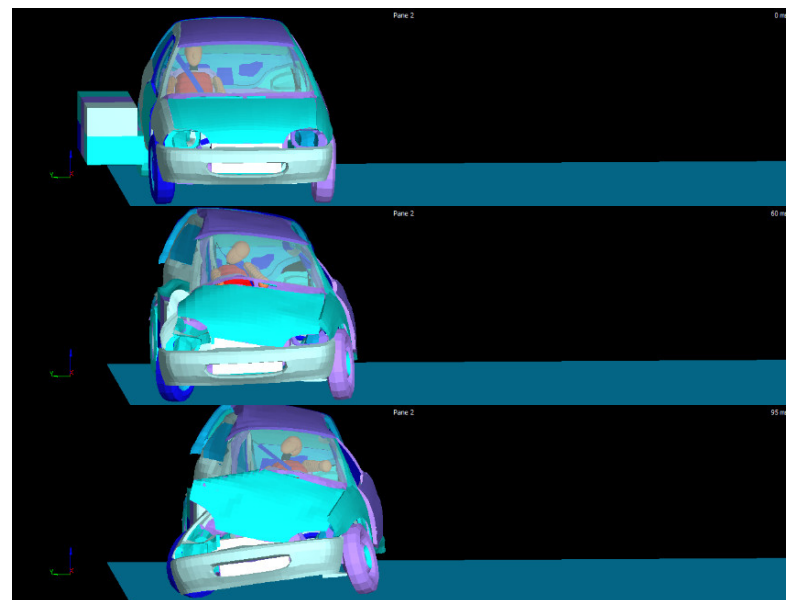


Figure 21. Kinematics of passenger in combustion vehicle subjected to a lateral collision according to ECE Regulation R95, using the ES-2 dummy.

3.3.2. Passenger Kinematics in an Electric Vehicle: Configuration 1

Figure 22 shows a sequence of frames showing the movement experienced by the passenger of an electric vehicle configuration 1 subjected to a lateral collision according to ECE Regulation R95.

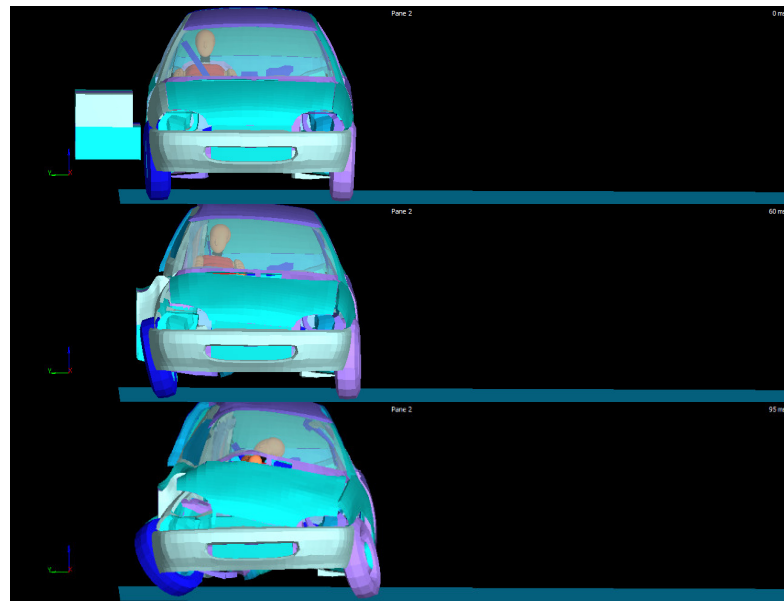


Figure 22. Kinematics of passenger for electric vehicle configuration 1 subjected to a lateral collision according to ECE Regulation R95, using the ES-2 dummy.

3.3.3. Passenger Kinematics in Electric Vehicle: Configuration 2

Figure 23 shows a sequence of frames showing the movement experienced by the passenger of an electric vehicle configuration 2 subjected to a lateral collision according to ECE Regulation R95.

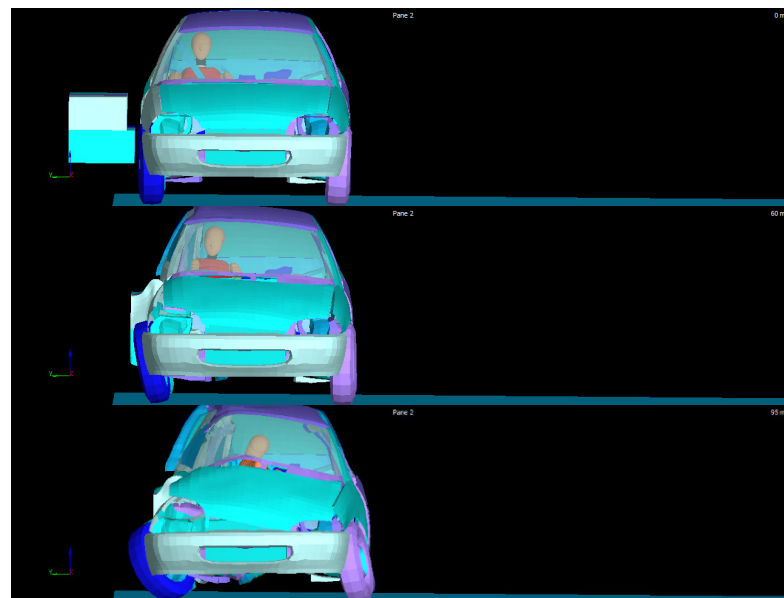


Figure 23. Kinematics of passenger for electric vehicle configuration 2 subjected to lateral collision according to ECE Regulation R95, using the ES-2 dummy.

3.3.4. Passenger Kinematics in Electric Vehicle: Configuration 1 with Energy Absorbers

Figure 24 shows a sequence of frames showing the movement experienced by the passenger of an electric vehicle configuration 1 with energy absorbers, subjected to a lateral collision according to ECE Regulation R95.

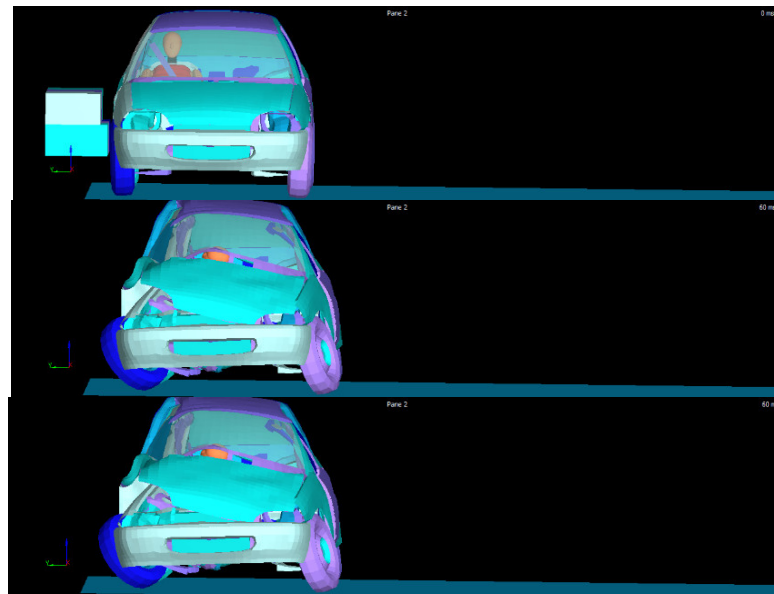


Figure 24. Kinematics of passenger for electric vehicle configuration 1 with energy absorbers, subjected to a lateral collision according to ECE Regulation R95, using the ES-2 dummy.

3.3.5. Passenger Kinematics in Electric Vehicle: Configuration 2 with Energy Absorbers

Figure 25 shows a sequence of frames showing the movement experienced by the passenger of an electric vehicle configuration 2 with energy absorbers, subjected to a lateral collision according to ECE Regulation R95.

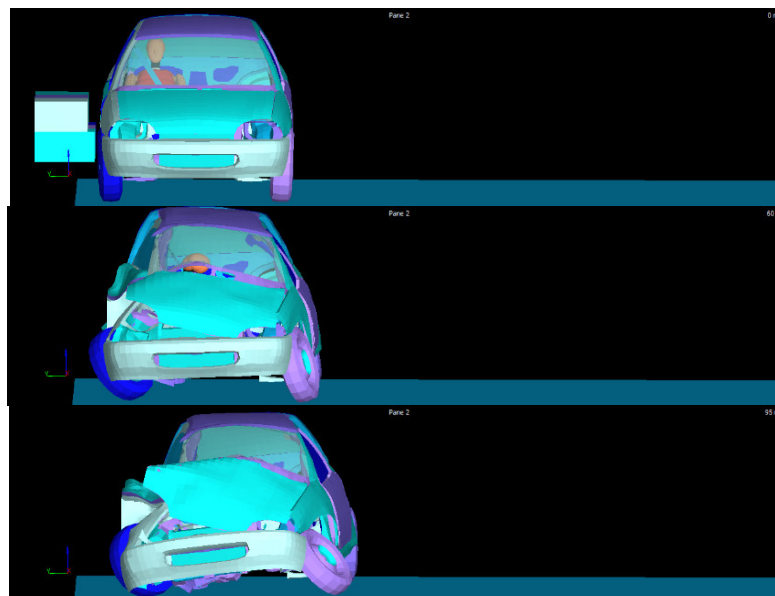


Figure 25. Kinematics of passenger for electric vehicle configuration 2 with energy absorbers, subjected to a lateral collision according to ECE Regulation R95, using the ES-2 dummy.

A comparison of the movement (Figure 26) showed that with a combustion vehicle, the deformation of the lower part of the vehicle is increased, and the occupant moves more to the side opposite to the impact side. For configurations 1 and 2 with energy absorbers, the occupant moves more toward the side opposite to the impact side than in the cases of the configurations without absorbers. This occurs because the traction battery with absorbers stiffens the area and when shock absorbers are not included, it has a small clearance that

allows it to deform and not directly receive the impact. With absorbers, no space exists before the traction battery plus absorbers assembly is impacted.

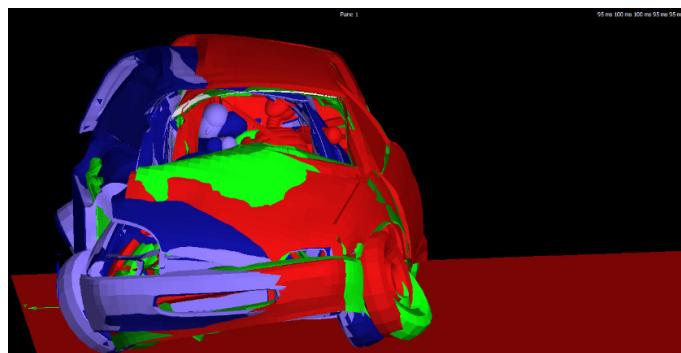


Figure 26. Passenger kinematic comparison for different vehicle configurations.

3.4. Influence of Battery Layout on Risk of Injury

The influence of battery layout and the presence or absence of energy absorbers on the risk of injury to the passenger is explained below.

3.4.1. Analysis of Head Injuries

According to ECE Regulation R95, the head performance criterion (CCC) applies when contact occurs with the head in a crash. The CCC is the maximum value of the following Formula (1):

$$(t_2 - t_1) \left(\frac{1}{t_2 - t_1} \int_{t_1}^{t_2} a \, dt \right)^{2.5} \tag{1}$$

where a is the resulting acceleration at the center of gravity of the head, in meters per second squared, divided by 9.81, measured as a function of time and filtered with a channel frequency class of 1000 Hz; t_1 and t_2 are any two moments between the initial and final contact.

This formula corresponds to the head injury criterion (HIC) (2):

$$HIC = \max_{T_0 \leq t_1 \leq t_2 \leq T_E} \left[\frac{1}{t_2 - t_1} \int_{t_1}^{t_2} R(t) dt \right]^{2.5} (t_2 - t_1) \tag{2}$$

where t_1 is the start time, t_2 is the end time, and $R(t)$ is $a(t)$, the acceleration curve experienced by the struck head, where (t) is measured in seconds and a is measured in g 's.

A value of 1000 is cited as the injury threshold in aviation regulations. First, the HIC calculation was limited to a 36 ms interval (HIC_{36}) with an injury threshold of 1000. Subsequently, it was revised, limiting the maximum time interval to 15 ms and reducing the injury threshold to 700 (referred to as HIC_{15}). An HIC_{15} value of 700 represents a 5% risk of serious injury or an abbreviated injury scale (AIS) of 4.

The CCC should be less or equal to 1000 when no head contact occurs. In that case, the CCC is not measured or calculated. Instead, "no head contact" is indicated.

Table 14 shows the HIC_{36} value for each of the configurations analyzed.

Table 14. HIC_{36} experienced by the dummy for each of analyzed configurations.

	Without Battery	Config. 1	Config. 2	Config. 1 with Shock-Absorbing Elements	Config. 2 with Shock-Absorbing Elements
HIC_{36}	37.972	13.424	20.681	113.706	79.038

The values are well above the injury threshold (1000), which is why the curtain airbag and the side airbag have been included in vehicles.

To explain the difference among the HIC in the different configurations, the acceleration experienced by the head of the dummy in each configuration was analyzed.

Figure 27 shows how the maximum acceleration value experienced by the occupant of a combustion vehicle is reduced when a traction battery is added. Moreover, this maximum deceleration is reached later. The lowest acceleration value is reached with configuration 1. However, by adding crash absorbers and reducing the space between the running board (where the deformable moving barrier is impacted) and the traction battery plus absorbers, the maximum value is reached earlier. However, when that area is stiffened, the maximum head acceleration value is higher.

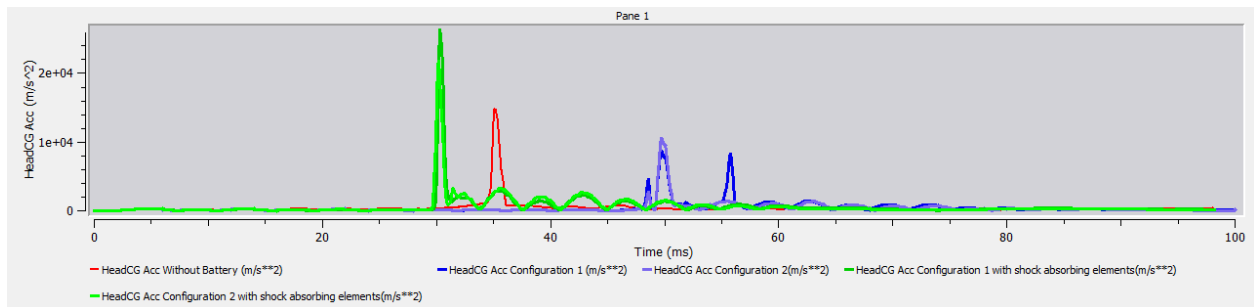


Figure 27. Comparison of head acceleration in each of analyzed configurations.

3.4.2. Analysis of Thorax Injuries

According to ECE Regulation R95, the maximum chest deformation is the maximum deformation value for any rib as determined by chest displacement transducers, filtered with a channel frequency of 180 Hz.

The viscosity criterion is applied. The maximum viscosity is the maximum value for the viscosity criterion at any rib, calculated from the instantaneous product of the relative compression of the thorax with respect to the semithorax and the compression speed derived by compression differentiation, filtered with a channel frequency of 180 Hz. The normalized width of the half-thoracic cage is considered as 140 mm, where D (in meters) is the rib deformation:

$$VC = \max\left(\frac{D}{0.14} \cdot \frac{dD}{dt}\right) \quad (3)$$

The performance criteria for the thorax are as follows:

- In the case of the rib deformation criterion, less than or equal to 42 mm.
- In the case of the soft tissue criterion (viscosity criterion (VC), less than or equal to 1.0 m/s.

During a transitional period of two years from the date specified in the Regulation, the viscosity criterion value should not be a determining value for passing the approval test but should be recorded in the test report and registered by the approval authority. After the transitional period has elapsed, a viscosity criterion value of 1.0 m/s shall be applied as a pass.

The following chest injury criteria values (Table 15) were obtained in the upper, middle, and lower rib area with MADYMO software R2212:

VC value (Figure 28) in the upper part of the ribs is the lowest for configuration 2 and the highest value for configuration 1 with shock absorbers. In the middle part of the ribs, the VC value (Figure 29) is the lowest for configuration 2 with shock absorbers and the highest in of the combustion vehicle. In the lower part of the ribs, the VC value (Figure 30) is the lowest for configuration 2 with shock elements and the highest for configuration 2.

Table 15. Rib compression and viscosity criterion (VC) for each of analyzed configurations.

	Without Battery	Config. 1	Config. 2	Config. 1 with Shock-Absorbing Elements	Config. 2 with Shock-Absorbing Elements
Upper Rib Compr. (mm)	59.47	52.24	55.08	75.90	67.26
Mid Rib Compr. (mm)	69.51	46.13	48.39	48.82	42.25
Lower Rib Compr. (mm)	68.70	56.66	64.15	38.37	30.18
Upper Rib VC (m/s)	1.57	1.38	1.33	3.71	2.61
Mid Rib VC (m/s)	1.94	1.15	1.34	1.46	1.03
Lower Rib VC (m/s)	2.14	1.78	2.43	1.06	0.57

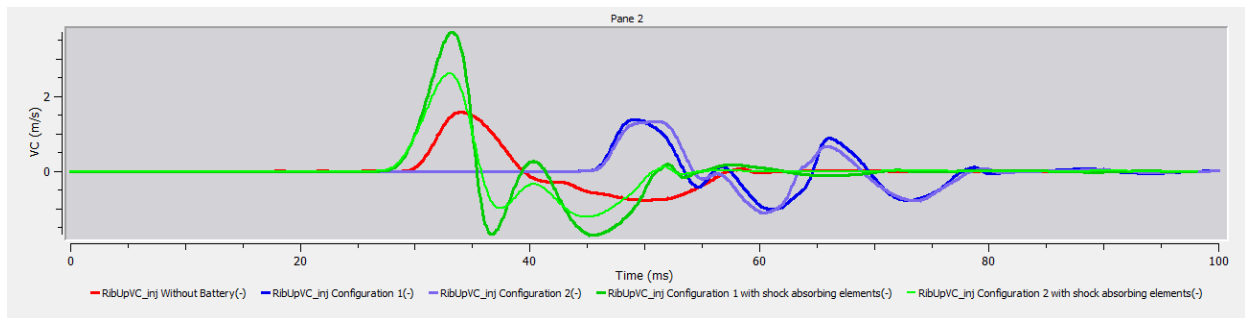


Figure 28. VC at upper ribs for each of the configurations analyzed.

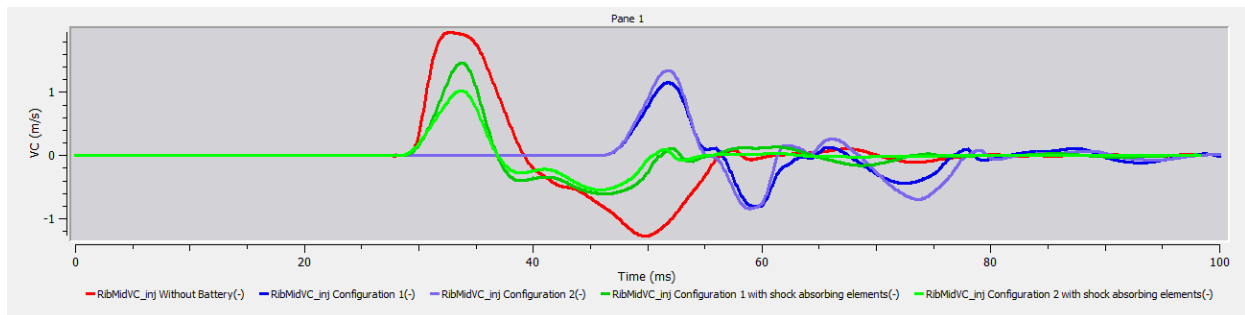


Figure 29. VC at middle ribs for each of the configurations analyzed.

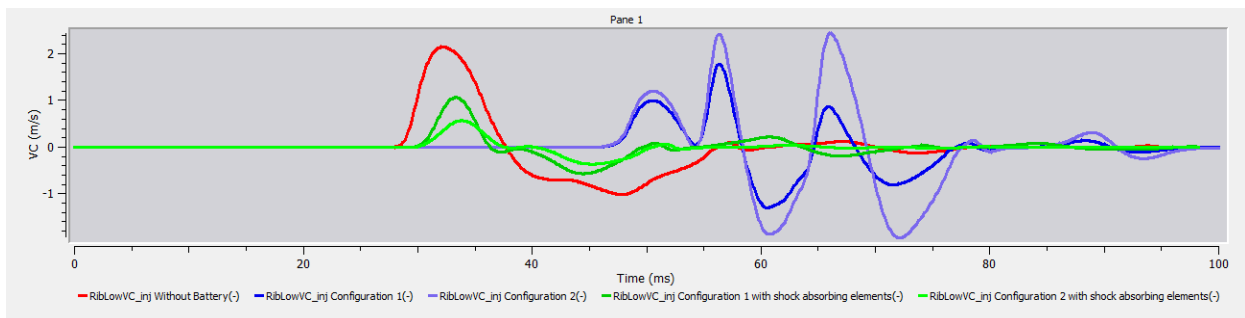


Figure 30. VC at lower ribs for each of the configurations analyzed.

3.4.3. Analysis of Abdomen Injuries

According to ECE Regulation R95, the maximum force on the abdomen is the maximum value of the sum of the three forces measured by transducers mounted 39 mm below the surface of the impacted side, with a CFC of 600 Hz.

The abdominal performance criterion according to ECE Regulation R95 states that the maximum force on the abdomen must be less than or equal to 2.5 kN of internal force (equivalent to an external force of 4.5 kN).

In the Table 16 it is noted that the inclusion of the traction battery considerably reduces the value of the maximum force in the abdomen (APF), reaching values that are below the injury threshold value (2.5 kN). The minimum value is reached with configuration 1.

Table 16. APF value (maximum force in the abdomen) for each of the configurations analyzed.

	Without Battery	Config. 1	Config. 2	Config. 1 with Shock-Absorbing Elements	Config. 2 with Shock-Absorbing Elements
APF (N)	9168.0	1277.0	1539.9	1707.0	1558.9

Figure 31 shows the APF value for each of the configurations analyzed.

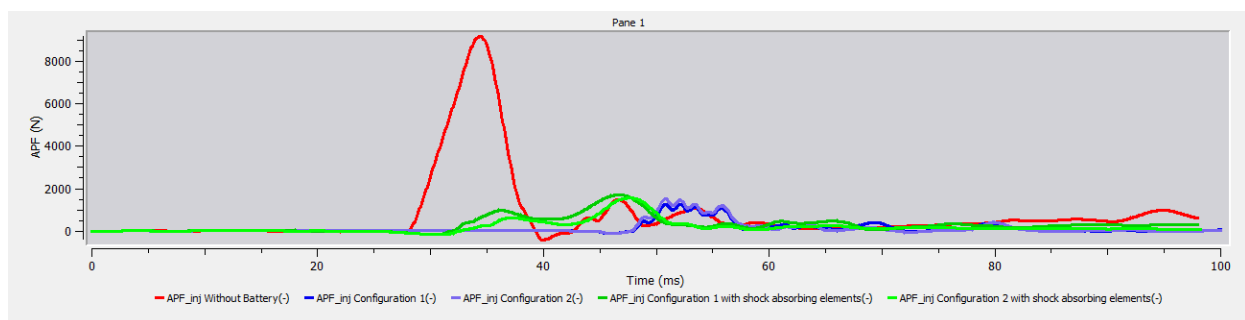


Figure 31. APF value for each of the configurations analyzed.

3.4.4. Analysis of Pelvis Injuries

According to ECE Regulation R95, the maximum force on the pubic symphysis is the maximum force measured with a load cell on the pubic symphysis of the pelvis, filtered with a channel frequency of 600 Hz.

The criterion for the pelvic behavior according to ECE Regulation R95 states the maximum force on the pubic symphysis must be less than or equal to 6 kN.

In the Table 17 it is noted that the traction battery, regardless of the configuration, reduces the PSPF value. However, the PSPF is below the injury threshold (6 kN) for all cases. The lowest PSPF value is achieved with configuration 2 with shock absorbers.

Table 17. Maximum value of maximum force on pubic symphysis (PSPF) for each of the configurations analyzed.

	Without Battery	Config. 1	Config. 2	Config. 1 with Shock-Absorbing Elements	Config. 2 with Shock-Absorbing Elements
PSPF (N)	5792.11	4.609.2	4.864.3	3.323.9	2.642.9

Figure 32 shows the PSPF value for each of the configurations analyzed.

The modifying parameters of the EuroNCAP assessment protocol, backplate force, T_{12} vertebra force, and T_{12} vertebra moment were also obtained (Table 18).

We observed that the inclusion of the traction battery reduces the value of the force on the backplate, reaching the lowest value in the case of configuration 1 (Figure 33).

We observed that the inclusion of the traction battery reduces the F_y of the T_{12} vertebra (Figure 34), reaching the lowest value for configuration 1, and reduces the M_x of the T_{12} vertebra, reaching the lowest value for configuration 1 (Figure 35).

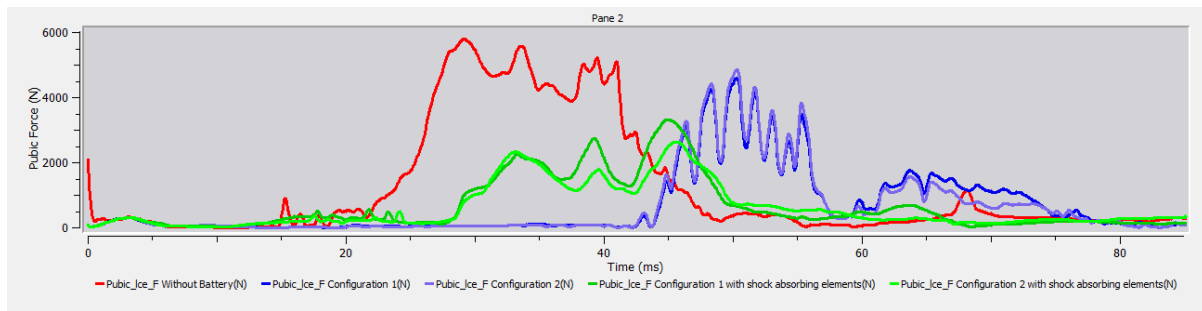


Figure 32. PSPF value for each of the configurations analyzed.

Table 18. Value of the modifier parameters for each of the configurations analyzed.

	Without Battery	Config. 1	Config. 2	Config. 1 with Shock-Absorbing Elements	Config. 2 with Shock-Absorbing elements
F_y force in backplate	3648.2	797.77	1194.1	3722.3	954.81
F_y force in T₁₂	10,493.0	3161.2	5071.2	7036.6	6576.8
M_x torque in T₁₂	630.57	305.85	310.55	379.45	335.50

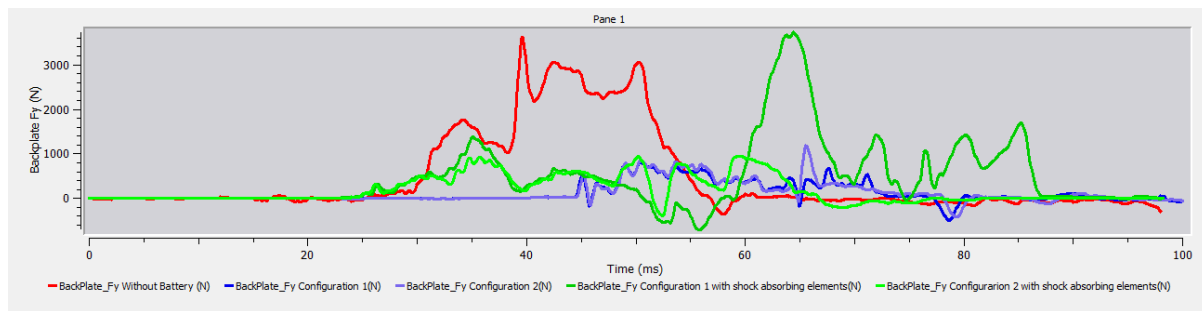


Figure 33. F_y in backplate for each of the configurations analyzed.

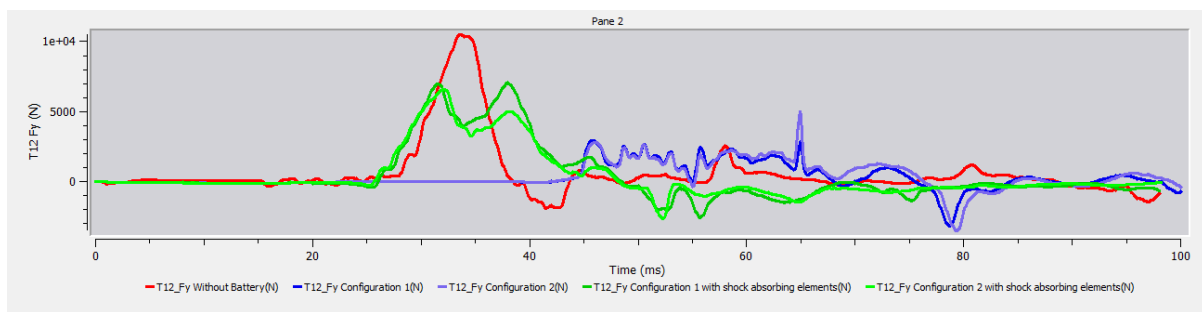


Figure 34. F_y at the T₁₂ vertebra for each of the configurations analyzed.

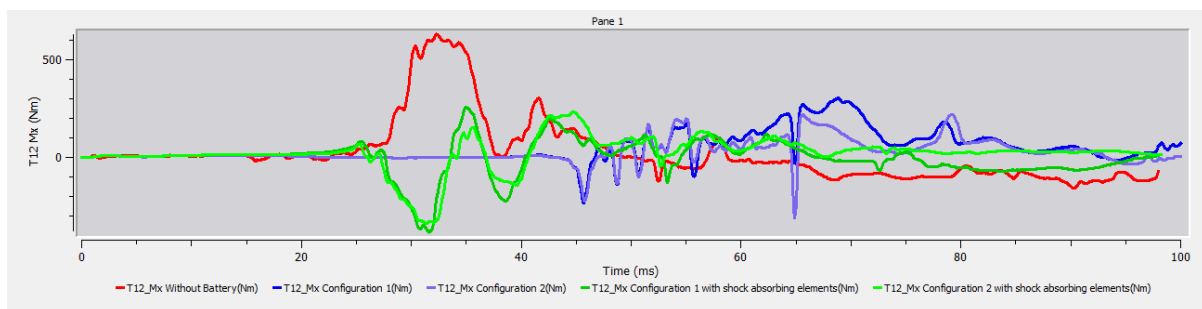


Figure 35. M_x at the T₁₂ vertebra for each of the configurations analyzed.

4. Conclusions

After analyzing the results obtained for each configuration (initial vehicle without battery, configurations 1 and 2 with battery, and both configurations with battery plus absorbers), the following conclusions were drawn:

- By including the battery pack in the vehicle, the stiffness of the car floor is increased, resulting in smaller intrusions into the passenger compartment, which implies an increase in occupant safety.
- None of the configurations showed the ability to prevent thermal runaway. For all cases, the most critical module type is the one with the largest surface area facing the direction of impact.
- The best option for electrifying the Geo Metro model is configuration 1 with shock absorbers because the smallest intrusions into the passenger compartment are obtained.
- Although the second configuration has a distribution of the modules that minimizes heat transmission in case of thermal runaway, it performs worse than the first configuration because it is narrower.
- The materials chosen for the body of the model (DOCOL1000 steel) and the battery casing (DC01 steel) proved to be insufficiently resistant to side impacts for some of the configurations.
- When comparing the movement, we observed that for the combustion vehicle, the deformation of the lower part of the vehicle is larger, and the occupant moves more toward the opposite side from the impact. In configurations 1 and 2 with absorbers, the occupant moves more toward the side opposite the impact than in the two configurations without absorbers. This is because the traction battery with absorbers stiffens the area and, without absorbers, has a small clearance that allows it to deform and not directly receive the impact.
- By including the battery pack in the vehicle, the maximum acceleration value at the occupant head is reduced and reached later. Configuration 1 is the case where the maximum acceleration at the occupant's head is reduced the most. However, by adding the absorbers and reducing the space between the running board and the traction battery plus absorbers, the maximum value is reached earlier. By stiffening the area, the maximum head acceleration value is higher.
- The VC value is also reduced when the battery pack is included. Its lowest value is reached at the upper part of the ribs for configuration 2. However, the lowest value at the middle part of the ribs corresponds to configuration 2 with absorbers. Moreover, the lowest value for the lower part of the ribs occurs with configuration 2 with absorbers.
- The inclusion of the traction battery also considerably reduces the maximum force in the abdomen (APF), reaching values that are below the injury threshold (2.5 kN). The minimum value is reached with configuration 1.
- Including the traction battery reduces the PSPF; in all configurations, the values are below the injury threshold (6 kN). The configuration with the lowest PSPF is configuration 1 with absorbers.
- Including the traction battery also reduces the F_y in the backplate and T12, and reduces the value of M_x in T12, reaching the lowest value of the three analyzed variables for configuration 1.
- Considering all the results, the best option for electrifying the studied Geo Metro car is configuration 1, which results in the least injuries to the right-front occupant.
- No direct impact to the battery pack occurs for any configuration. This demonstrates that the compact designs proposed in this project enables the implementation of a narrow battery that does not suffer a direct collision. In addition, the structural elements of the vehicle and the components of the battery pack can absorb the impact energy so that the impact does not hit the modules. However, in general, when energy absorbers are included, the loads suffered by the occupant are reduced.

Because thermal runaway is initiated in the same type of module in all configurations, the modules facing the impact direction must be protected from deformations above the defined maximum shortening. For this purpose, one or more of the following solutions can be implemented:

- Change the material of the module shells and/or increase their thickness.
- Reinforce the battery casing by changing the material or increasing their thickness.
- Increase the energy absorbed by deformation before it reaches the modules through thicker shock-absorbing elements (limited option to the space available).
- Include absorption elements inside the doors, closer to the impact area, ensuring their effectiveness and thus further reducing intrusion into the passenger compartment during impact.
- Place a thin absorber element between the floor of the housing and the floor of the vehicle to reduce the stresses on the battery and the stresses produced when rolling over uneven ground, providing cushioning.
- Avoid contact between the casing and the ground by raising the casing. This could be combined with a bar structure under the battery, which would additionally provide stiffness to the vehicle floor.
- Perform additional studies on absorbers to further reduce the stresses on the occupant.
- To reduce head and rib injuries, incorporate restraint and protection systems such as curtain airbags or side airbags, as well as absorber elements in the door panel.

Author Contributions: Conceptualization, A.O. and L.C.; data curation, A.O. and L.C.; formal analysis, A.O. and L.C.; funding acquisition, A.O. and L.C.; investigation, A.O., L.C. and D.V.; methodology, A.O. and D.V.; project administration, L.C.; resources, A.O., L.C. and D.V.; supervision, L.C.; writing—original draft, A.O. and L.C.; writing—review and editing, A.O. All authors have read and agreed to the published version of the manuscript.

Funding: This research was funded by University of Zaragoza: Industrial Doctorate (DI 4/2020).

Data Availability Statement: The data presented in this study are available on request from the corresponding author. The data are not publicly available due to restrictions privacy.

Acknowledgments: The authors are grateful for the support received through the Industrial Doctorate financed by the University of Zaragoza (DI 4/2020) and Instituto de Investigación sobre Vehículos, S.A. (Centro Zaragoza), in which the work presented in this article was framed.

Conflicts of Interest: The authors declare no conflict of interest.

References

1. Kukreja, J.; Nguyen, T.; Siegmund, T.; Chen, W.; Tsutsui, W.; Balakrishnan, K.; Liao, H.; Parab, N. Crash analysis of a conceptual electric vehicle with a damage tolerant battery pack. *Extrem. Mech. Lett.* **2016**, *9*, 371–378. [[CrossRef](#)]
2. Feng, X.; Ouyang, M.; Liu, X.; Lu, L.; Xia, Y.; He, X. Thermal Runaway mechanism of lithium ion battery for electric vehicles: A review. *Energy Storage Mater.* **2018**, *10*, 246–267. [[CrossRef](#)]
3. Dirección General de Tráfico (DGT). *Siniestralidad Mortal en Vías Interurbanas 2022 (Cómputo de Personas Fallecidas a 24 Horas): Datos Provisionales*; Observatorio Nacional de Seguridad Vial: Madrid, Spain, 2023.
4. NHTSA, U.S. Department of Transportation, National Highway Traffic Administration. *Laboratory Test Procedure for FMVSS No. 214, Dynamic Side Impact Protection*; NHTSA, U.S. Department of Transportation, National Highway Traffic Administration: Washington, DC, USA, 2012.
5. Crash Regulations Overview. Overview of Legislative/Consumer Crash Regulations and Insurance Ratings. Available online: <https://static.qichecailiao.com/201507/29/20-01-49-44-2.pdf> (accessed on 5 September 2023).
6. Bahouth, G.T.; Murakhovskiy, D.; Digges, K.H.; Rist, H.; Wiik, R. Opportunities for reducing far-side casualties. In *Proceedings of the 24th International Technical Conference on the Enhanced Safety of Vehicles (ESV)*, Gothenburg, Sweden, 8–11 June 2015; National Highway Traffic Safety Administration: Washington, DC, USA, 2015.
7. Gabler, H.C.; Michael, F.; James, S.; Brian, N.F.; Kennerly, D.; Laurie, S. Far-side impact injury risk for belted occupants in Australia and the United States. In *Proceedings of the 19th International Conference on Enhanced Safety of Vehicles*, Washington, DC, USA, 6–9 June 2005.

8. Triumph. El reto: Una Fabricación Rentable y Fiable en Cuanto a los Procesos de Baterías de Iones Litio de alto Rendimiento para la Electromovilidad. 2023. Available online: https://www.trumpf.com/es_MX/soluciones/sectores/automocion/electromovilidad/celdas-de-bateria-y-modulos/ (accessed on 12 April 2023).
9. Marklines. *Nissan Leaf Teardown: Lithium-ion Battery Pack Structure*. 2023. Available online: https://www.marklines.com/en/report_all/rep1786_201811 (accessed on 12 April 2023).
10. Maluf, N. Qnovo. 2023. Available online: <https://www.qnovo.com/blogs/inside-the-battery-of-a-nissan-leaf> (accessed on 12 April 2023).
11. Wang, Z.; Mao, N.; Jiang, F. Study on the effect of spacing on thermal runaway propagation for lithium-ion battery. *Environ. Sci. Eng. J. Therm. Anal. Calorim.* **2019**, *140*, 2849–2863. [CrossRef]
12. Setiawan, R.; Salim, M.R. Crashworthiness Design for an Electric City Car against Side Pole Impact. *J. Eng. Technol. Sci.* **2017**, *49*, 587–603. [CrossRef]
13. Air Force and Naval Air Systems Command. *Technical Manual. Engineering Series for Aircraft Repair*. 1967. *Aerospace Metals—General Data and Usage Factors. TO 1-1A-9. TM 43-0106 Navair 01-1A-9*; Published under authority of the secretary of the Air Force and by direction of the Chief of the Naval Air Systems Command; Air Force and Naval Air Systems Command: Patuxent River, MD, USA, 2016.
14. Knight Group. Acero Dulce y Acero de Carbono. 2017. Available online: <https://www.knight-group.co.uk/wp-content/uploads/PM%20Files/Spanish/Materials/PMQR78%20Spanish%20Knight%20Group%20Carbon%20and%20Mild%20Steels.pdf> (accessed on 12 April 2023).
15. Nizam, M.; Sahay, A. Wrinkling Defect in Sheet Metal Process using Finite Element Analysis. *Int. J. Res. Appl. Sci. Eng. Technol.* **2022**, *10*, 4425. [CrossRef]
16. ASM International. *Volume 2: Properties and Selection: Nonferrous Alloys and Special-Purpose Materials*; ASM International: Arlington, VA, USA, 1990.
17. Yue, Q.; Louis, G.H.; Christine, J. Lithium Concentration Dependent Elastic Properties of Battery Electrode Materials from First Principles Calculations. *J. Electrochem. Soc.* **2014**, *161*, F3010–F3018.
18. Siemens. *Simcenter MADYMO Model Manual*; Siemens Version 2212 Model Manual; Siemens Industry Software Netherlands BV: Eindhoven, The Netherlands, 2022; p. 151.
19. Mallick, S.; Gayen, D. Thermal behaviour and thermal runaway propagation in lithium-ion battery systems—A critical review. *J. Energy Storage* **2023**, *62*, 106894. [CrossRef]
20. Li, A.; Weng, J.; Yuen, A.C.Y.; Wang, W.; Liu, H.; Lee, E.W.M.; Wang, J.; Kook, S.; Yeoh, G.H. Machine learning assisted advanced battery thermal management system: A state-of-the-art review. *J. Energy Storage* **2023**, *60*, 106688. [CrossRef]
21. Yang, S.; Ling, C.; Fan, Y.; Yang, Y.; Tan, X.; Dong, H. A Review of Lithium-Ion Battery Thermal Management System Strategies and the Evaluate Criteria. *Int. J. Electrochem. Sci.* **2019**, *14*, 6077–6107. [CrossRef]
22. Brooke, L. SAE International. 2021. Available online: <https://www.mobilityengineeringtech.com/component/content/article/ae/pub/features/articles/45150?r=40733> (accessed on 9 May 2023).
23. Usón, L. *Battery Protective Frame Optimization for an Electric Vehicle*; TFG Zaragoza University/School of Engineering and Architecture: Saragossa, Spain, 2022.

Disclaimer/Publisher’s Note: The statements, opinions and data contained in all publications are solely those of the individual author(s) and contributor(s) and not of MDPI and/or the editor(s). MDPI and/or the editor(s) disclaim responsibility for any injury to people or property resulting from any ideas, methods, instructions or products referred to in the content.